ADVANCED MATERIALS INTERFACES
Open Access
www.advmatinterfaces.de

Insight into the Impact of Electrolyte on Passivation of Lithium–Sulfur Cathodes

*Walter Cistjakov, Johanna Hoppe, Jinkwan Jung, Fridolin Röder, Hee-Tak Kim, and Ulrike Krewer**

One of the remaining challenges for lithium–sulfur batteries toward practical application is early cathode passivation by the insulating discharge product: Li_2S. To understand how to best mitigate passivation and minimize related performance loss, a kinetic Monte–Carlo model for Li_2S crystal growth from solution is developed. The key mechanisms behind the strongly different natures of Li_2S layer growth, structure, and morphology for salts with different (DN) are revealed. LiTFSI electrolyte in dimethyl ether leads to lateral Li_2S growth on carbon and fast passivation because it increases the Li_2S precipitation-to-dissolution probability on carbon relative to Li_2S. In contrast, LiBr electrolyte has a higher DN and yields a particle-like structure due to a significantly higher precipitation-to-dissolution probability on Li_2S compared to carbon. The resulting large number of Li_2S sites further favors particle growth, leading to low passivation. This study is able to identify the key parameters of the electrolyte and substrate material to tune Li_2S morphology and growth to pave the way for optimized performance.

1. Introduction

Increasing demand for sustainable, low-cost, and high gravimetric energy storage motivates research and development on next-generation batteries. Lithium–sulfur batteries (LSBs) are attractive alternatives to Lithium-ion batteries (LIBs) due to their high gravimetric energy density, with practical values reaching 400 Wh kg^{-1}. They also feature high environmental sustainability, low cost, and widespread abundance of the active material, sulfur. LSBs are already available in niche applications,[1] however, their widespread application is still inhibited due to performance issues caused by the insulating nature of their charge product (S_8) and discharge product (Li_2S), as well as self-discharge caused by the diffusion and migration of soluble intermediates, that is, polysulfides, between the anode and cathode. These processes result in low sulfur utilization in the whole cell, volume expansion of the cathode, low cycle number, and low coulombic efficiency.

To overcome these challenges, research has focused on understanding and controlling dissolved polysulfides and their electrochemical and chemical reactions, as well as on the deposition and dissolution of the charge/discharge products, sulfur and lithium sulfide. Several works have designed cathode frameworks to enclose polysulfides within porous carbon,[2,3] or graphene[4] structures, or to suppress the dissolution and diffusion of polysulfides with gel polymers.[5] These approaches showed progress in improving sulfur utilization, but challenges in preventing surface passivation still remain.

Other studies have investigated the precipitation of Li_2S on a substrate material, such as carbon or graphene, in order to identify the underlying mechanisms of passivation. Noh et al.[6] revealed experimentally how the discharge rate influenced the Li_2S precipitate structure at the carbon surface; high currents

W. Cistjakov
Institute of Energy and Process Systems Engineering
Technische Universität Braunschweig
Langer Kamp 19b, Braunschweig 38106, Lower Saxony, Germany
W. Cistjakov, J. Hoppe, U. Krewer
Cluster of Excellence "SE2A – Sustainable and Energy-Efficient Aviation"
Technische Universität Braunschweig
Hermann-Blenk-Str. 42, Braunschweig 38108, Lower Saxony, Germany
E-mail: ulrike.krewer@kit.edu

The ORCID identification number(s) for the author(s) of this article can be found under https://doi.org/10.1002/admi.202400632

DOI: 10.1002/admi.202400632

J. Hoppe
Transformation Pathways
Potsdam Institute for Climate Impact Research (PIK)
Telegrafenberg A 3, Potsdam 14412, Brandenburg, Germany
J. Jung, H.-T. Kim
Department of Chemical and Biomolecular Engineering
Korean Advanced Institute of Science and Technology
291 Daehak-ro, Daejeon 34141, South Korea
F. Röder
Bavarian Center for Battery Technology (BayBatt)
University of Bayreuth
Weiherstraße 26, Bayreuth 95448, Bavaria, Germany
U. Krewer
Institute for Applied Materials – Electrochemical Technologies
Karlsruhe Institute of Technology
Adenauerring 20b, Karlsruhe 76131, Baden-Wuerttemberg, Germany

resulted in the formation of numerous randomly distributed Li_2S islands, which coalesced into an amorphous structure on the carbon surface. In contrast, low currents allowed enough time for the species to coordinate and form a flat crystalline Li_2S surface on carbon, which resulted in early passivation during discharge. In addition, high discharge rates were also found to be better for cyclability because the amorphous Li_2S was more readily dissolved, which resulted in charge overpotentials. Temperature was also shown to impact Li_2S deposition; Lang et al.[7] compared the cyclability at room temperature and 60 °C for a 1:1 mixture of 1,2-dimethoxyethane (DOL) and 1,3-dioxolane (DME) with lithium bis-(fluorosulfonyl)imid (LiFSI) conductive salt. Here, they showed better cyclability at high temperatures. LiF is produced from LiFSI degradation in significant amounts at 60 °C, where it fills in the nanocavities of the Li_2S/Li_2S_2 structure and forms a solid film; this film captures polysulfides effectively while retaining good Li^+ conductivity. After each cycle, almost all solids are removed from the surface. In contrast, at room temperature, only crystalline Li_2S was precipitated and little LiF was produced. As a result, the solid and poorly soluble Li_2S_2 accumulates after each cycle leading to an electrically insulating layer.

In a different approach to mitigate surface passivation, Chu et al.[8] changed the electrolyte salt to control the shape of Li_2S precipitates formed during discharge. The widely used DOL: DME (1:1) electrolyte with a lithium bis(trifluoromethane sulfonyl)imide (LiTFSI) conductive salt has a low donor number and low Li_2S solubility; resulting in a flat Li_2S structure at the surface of the carbon substrate material after discharge. To prevent this detrimental structure, which leads to rapid passivation, Chu et al. replaced the conductive salt with the high donor number salt, lithium bromide (LiBr). This high doner number salt features a high solubility for Li_2S. This high solubility leads to a beneficial 3D particle-like Li_2S structure, slower passivation, and a higher discharge capacity compared to the LiTFSI electrolyte. Lang et al.[9] compared LiTFSI and LiFSI in DOL: DME. They confirmed the flat growth structure in cells with LiTFSI-based electrolytes, and they showed that cells with LiFSI-based electrolytes formed spherical Li_2S particles. The mechanisms of how these structures form and evolve over time are mostly speculative due to experimental limitations.

Mechanistic models that range from the atomic- to macroscale are increasingly used for understanding and optimizing the processes in LSBs, including passivation.[10] Liu et al.[11] used density functional theory (DFT) to investigate the growth of the insoluble species, Li_2S and Li_2S_2, on a crystalline Li_2S surface. They found that Li_2S is energetically favored over Li_2S_2 to deposit on (111) and (110) Li_2S surfaces. Park et al.[12] employed first-principles calculations to confirm the existence of Li_2S_2 as only a metastable phase that was directly transformed to Li_2S, and that the (111) surface is more prone to Li_2S crystal growth. Furthermore, Liu et al.[13] investigated the deposition of lithiated polysulfides on silicene and graphene with a method that couples coupling DFT calculations and kinetic Monte–Carlo (kMC) approach. They found that silicene can mitigate the polysulfide shuttle but induces faster surface passivation due to the higher attractive forces of Li_2S with the surface. In a further study, they used their kMC approach to investigate the influence of temperature and S^{2-} concentration on graphene surface passivation.[14] Andritos et al.[15] investigated doping graphene to increase the graphene binding energy to mitigate the polysulfide shuttle. A 3D kMC approach was proposed by Thangavel et al.,[16] in which they simulated a cathode with all soluble and insoluble sulfur species they defined. They showed the transport of polysulfides and the production of Li_2S close to the carbon particles for high and low discharge rates. So far, no molecular or kMC simulation studies have addressed why there are different Li_2S crystal structures or examined the significant influence of electrolyte solubility and concentration on the precipitation process.

On the macroscale, most simulation studies have focused on the electrochemical reactions and transport of dissolved polysulfides,[17–19] Schön et al.[20] revealed the complex interplay of chemical and electrochemical reactions by using a kinetic model containing seven reaction steps and diffusion. They also observed the early onset of Li_2S precipitation. The works by Ren et al.,[21] Xiong et al.[22] and Danner et al.[23] have analyzed the precipitation of the insoluble products S_8 and Li_2S and the resulting structures. They focused on determining the effect of discharge on the formation of spherical Li_2S particles with different radii. For this purpose, they have used constant reaction rates of Li_2S or the classical theory of nucleation and growth.

Such continuum approaches suffer from the inability to represent the inherent stochastic nature and inhomogeneity of precipitation. Wehinger et al.[24] reviewed multiscale approaches, which combine, for example, kMC and continuum or DFT and kMC models; these help to show inhomogeneities in layer growth versus electrode thickness for LIB anodes.[25] These also reveal the impact of reaction versus transport on the local composition of the solid electrolyte interphase (SEI) formed on Li metal.[26] Ab-initio parameterized kMC models revealed the impact of electrolyte composition on the thickness and composition of the SEI on Li metal; higher salt concentrations lead to thinner SEIs.[27] Such models have not yet been used for analyzing LSBs.

The strong impact of electrolyte composition on Li_2S growth and the resulting precipitate structure observed by Chu et al.,[9,28] and Lang et al.[9] indicates that electrolyte composition tailoring is a highly promising pathway to enable high-performance and durable LSB cathodes. To our best knowledge, so far, no simulation work has investigated the effect of electrolyte composition on surface passivation. Such an analysis promises to provide important new insights into the growth mechanisms and governing processes of passivation layer formation, as well as their sensitivity to electrolyte, surface, and performance properties. In this work, we employ a kMC model of solution-mediated Li_2S crystal growth to study these behaviors and properties. The model integrates approaches from the field of growth kinetics of organic crystals to consider the electrolyte's interaction with the solid crystal surface,[29–31] These approaches studied the growth of a simple cubic system, the Kossel crystal, and applied it exemplarily to the crystallization of hexamethylenetetramine from an aqueous and alcoholic solution.[29] Here, we show that our model can reproduce the experimentally observed different Li_2S structures and morphologies for DME electrolytes with two different conductive salts, LiTFSI and LiBr. We will highlight the strongly different nature of the evolution of precipitation structures for both electrolytes, how the number of next Li_2S neighbors impacts growth, and how electrode surface properties impact the sensitivity to the electrolyte.

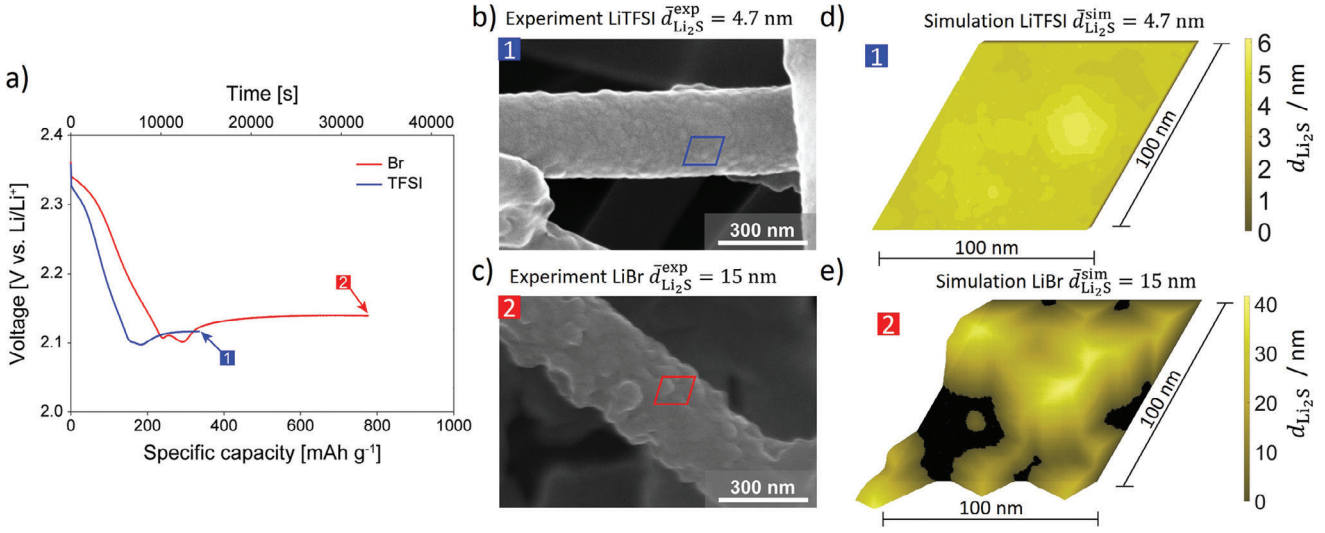

Figure 1. Electrochemical performance and cathode precipitate morphology for lithium–sulfur battery: a) Measured discharge curves at 0.05C for 1 M LiBr and LiTFSI. Experimental SEM images and average thickness of Li_2S precipitates on carbon nanofiber-based cathode after discharge for b) LiTFSI electrolyte and c) LiBr electrolyte. Discharge was terminated at half of the discharge capacity of the second plateau at 340 mAh g^{-1} for 1 M: LiTFSI, and 780 mAh g^{-1} for 1 M LiBr (cf. Figure S1, Supporting Information). Corresponding kMC simulation results of the Li_2S structure and average thickness at the carbon surface area for d) LiTFSI electrolyte and e) LiBr electrolyte. Parameters in **Table 1** were used.

2. Results

Understanding the impact of electrolyte salts on discharge performance and Li_2S precipitate morphology is at the center of this publication. The experimentally analyzed setup consists of lithium–sulfur cells with a carbon nanofiber cathode, a polypropylene separator, a lithium metal anode, and a DME electrolyte containing polysulfides with either LiBr or LiTFSI as salt. The electrolyte/polysulfide solution is prepared by dissolving Li_2S_8 into the electrolyte. Using dissolved Li_2S_8 instead of solid S_8 prevents the effects of solid S_8 at the surface. Discharge of the cell is stopped in the middle of the second voltage plateau, before complete passivation, to allow for better morphological analysis of Li_2S precipitate on the carbon surface. The experiments were used to parameterize the kMC simulations. For the derivation of mathematical model and experimental details see the Experimental Section (Section 4). The following sections will reveal the sensitivity of the precipitate morphology evolution to electrolyte and electrode properties by model-based scanning of the impact of a wide range of electrode and electrolyte properties.

2.1. Experimental versus Simulated Li_2S Morphology

The experimentally obtained discharge performance and Li_2S growth morphology for a low and a high donor number electrolyte are given in **Figure 1a–c**, respectively.

Both discharge curves show high voltages ≈2.33 V for a short time before dropping to 2.1 V and recovering to a second plateau ≈2.13 V. The voltage drop occurs more quickly with the LiTFSI electrolyte, and the voltage minimum is reached at a lower discharge capacity. The discharge is terminated at half of the discharge capacity of the second voltage plateau, 780 mAh g^{-1} for the LiBr electrolyte and 340 mAh g^{-1} for the LiTFSI electrolyte, determined by an earlier full discharge experiment (Figure S1, Supporting Information). Terminating the discharge at half of the discharge capacity of the second plateau timing was chosen to assess the Li_2S morphology on the carbon surface in a post-mortem analysis and to avoid complete passivation of the carbon surface. The predicted structures for full and half discharge are similar (Figure S1, Supporting Information), confirming the general trends discussed in the following. Further, comparison at the same capacity for both electrolytes would not be feasible as at the final capacity for the cell with LiTFSI the second plateau in the cell with LiBr, and thus precipitation, has not yet started. At the start of cell discharge for both electrolytes, long chain polysulfides (S_8^{2-}) react to shorter chains (S_4^{2-}) that cause the initial high voltage. According to Ghaznavi et al.,[17] the steep voltage drop can be attributed to the initiation of the reaction of S_4^{2-} to S^{2-}, which is followed by the precipitation of Li_2S, ultimately leading to the voltage plateau. The plateau is explained by an equal consumption-to-production ratio of S^{2-}, which leads to a constant S^{2-} concentration in the electrolyte bulk. The growth of the Li_2S precipitate on the carbon surface continues until the discharge is terminated. The experimentally obtained average Li_2S thickness on the carbon surface was 4.7 nm for the LiTFSI electrolyte and 15 nm for the LiBr electrolyte.

For the LiTFSI electrolyte, a flat, film-like Li_2S surface structure that fully covers the nanofiber surface is formed (Figure 1b, see also Figure S1d, Supporting Information for full discharge). No defined particle structures are recognizable. In contrast, the LiBr electrolyte yields a rough Li_2S surface structure with large round precipitates (Figure 1c, see also Figure S1e, Supporting Information for full discharge) with individual particle diameters that range from 49 to 85 nm.[8] The differences between flat structures for LiTFSI and the rough ones for LiBr salts are due to the larger solubility of Li_2S for LiBr.

Simulations on a 100 × 100 nm carbon surface accurately reproduced the experimentally observed morphology and average

Table 1. Material-specific parameter set for the simulation scenario for the LiTFSI and the LiBr electrolyte.

Symbol	Description	LiTFSI	LiBr	Unit
α_{111}	Surface roughness factor	16.549[a)]	6.0452[a)]	–
ΔP	Interfacial difference parameter	3.75[b)]	3.75[b)]	–
K_{sp}	Solubility product	10^{-3}[14]	5.958×10^{5}[a)]	$mol^3\ m^{-9}$
k_t	Frequency factor	2.497×10^{-4}[b)]	6.249×10^{-3}[b)]	s^{-1}
X_{Li_2S}	Molar fraction	1.048×10^{-13}[a)]	1.394×10^{-4}[a)]	$mol\ m^{-3}$
$c^{sat}_{Li_2S}$	Concentration of Li_2S in a saturated electrolyte	10^{-12}[a)]	1.33×10^{-3}[c)]	$mol\ m^{-3}$
$c^{salt}_{Li^+}$	Li^+ concentration from the conducting salt	10^{3}[14]	10^{3}[14]	$mol\ m^{-3}$
c_{S2-}	S^{2-} concentration during 0.05C discharge in precipitation phase	6.5×10^{-4}[b)]	40[b)]	$mol\ m^{-3}$

[a)] Calculated; [b)] Adjusted to reproduce experiments; [c)] Measured experimentally.

precipitate thickness, as seen in Figure 1d,e. Although the carbon support in the experiment consisted of round nanofibers, the assumption of a flat kMC surface is justified because the fibers were sufficiently large that their circumference of 946 nm was ≈10 times larger than the full kMC grid size, which would result in only a small curvature. Specific properties of the carbon will also enter the unknown model parameters, which were adjusted to reproduce the experiment: The identified parameters of the frequency factor k_t, the interfacial difference parameter ΔP and the S^{2-} concentration in the oversaturated solution $c_{S^{2-}}$ are given in Table 1. k_t, as a frequency factor, affects the precipitation time and is adjusted to reproduce the precipitation duration of the experiment. The calculation of the binding energy under vacuum conditions by Chu et al.[8] has been used to estimate ΔP. The higher binding energy of Li_2S on Li_2S layer (2.48 eV) shows higher binding affinity than on graphite (1.39 eV). This reveals that the ΔP can only be positive. Due to missing interaction energies we adjusted the value manually to $\Delta P = 3.75$ to reproduce the experimental results for the carbon nanofibers. For LiTFSI, the S^{2-} concentration of 6.5×10^{-4} mol m^{-3} was chosen that was close to the value of 10^{-3} mol m^{-3} predicted by the simulation study of Ghaznavi et al.[17] In contrast, LiBr electrolyte is able to dissolve more Li_2S due to its higher solubility, which is why S^{2-} was adjusted to 40 mol m^{-3}. Further parameters are material-specific properties that have been measured or calculated (see SI). As the only parameters determined from the experiments, that is, ΔP, k_t and $c_{S^{2-}}$, were applied for both electrolytes, differences in precipitation kinetics and morphology between the electrodes can be attributed to material parameters.

The kMC simulation using the LiTFSI electrolyte yielded an average Li_2S thickness of 4.7 ± 0.13 nm and a fully covered surface. The structure predicted by the simulation, a flat surface with small roughness, as well as the average Li_2S thickness, corresponds well with experimental results. The minimum Li_2S thickness is 3.3 nm, whereas the highest site is only 5.7 nm, indicating that lateral Li_2S precipitation is favored. Homogeneous layer growth can be assumed to continue during the second half of the discharge, with the thick insulating layer increasingly impeding electron transfer from the carbon surface. This leads to the experimentally observed voltage decrease and low practical capacity (cf. Figure S1, Supporting Information).

The simulation using LiBr yielded a surface area covered only 83% by Li_2S. The 15 nm average Li_2S thickness with a high standard deviation of 3.76 nm matches the particle-like structure in the experiments. Based on the simulation, Li_2S favors to precipitate on top of the Li_2S surface instead of on the carbon surface because of the higher energetical attraction of Li_2S molecules to each other (detailed analysis see sections below). This leads to the growth of particle-like structures of up to 40 nm and a high surface roughness. As there is still 17% free carbon surface area after half of a full discharge, this facilitates the reduction of sulfur species at a much lower depth of discharge for the LiBr electrolyte, which results in a higher sulfur utilization and higher practical capacities compared to the LiTFSI electrolyte.

In conclusion, our kMC model can reproduce the different Li_2S precipitate structures observed experimentally for electrolytes with 1 M LiTFSI versus LiBr. A particle-like structure is achieved for LiBr, in contrast to a flat surface structure obtained for the LiTFSI electrolyte. The particle-like structure allows for slower passivation; which enables a longer availability of electrons from the carbon surface for polysulfide reduction, which, in turn, explains the higher capacities observed experimentally. To understand why we see such different behavior for the salts, we look deeper into the evolution of the Li_2S morphology in the following section.

2.2. Evolution of Li_2S Morphology

We analyze the evolution of the structures from the beginning in order to determine how and why the different salts cause a difference in precipitate morphology. **Figure 2a** shows the evolution of the Li_2S surface coverage, Θ_{Li_2S}, that is, the fraction of the carbon surface covered by Li_2S precipitate, and the evolution of the average precipitate thickness $\bar{d}_{Li_2S}$, including their respective standard deviations, for the LiTFSI electrolyte.

Four stages are visible during the Li_2S precipitation process, similar to the analysis of Liu et. al.[14] Nucleation starts in the first phase, with negligible average thickness and coverage, with only single surface sites occupied by Li_2S (Figure 2a). Here, deposition and dissolution of Li_2S on the carbon surface occur at almost equal rates because not enough molecules congregate in one spot to form a stable nucleus. The Gibbs free energy state can be used to explain this process; for the single Li_2S molecules at the carbon surface, the energy to precipitate is close to that for dissolution. The concentration-, surface-, environment- and species-dependent Gibbs energies enter the transition rates for dissolution and precipitation (see Equations (1–4)). We analyze the

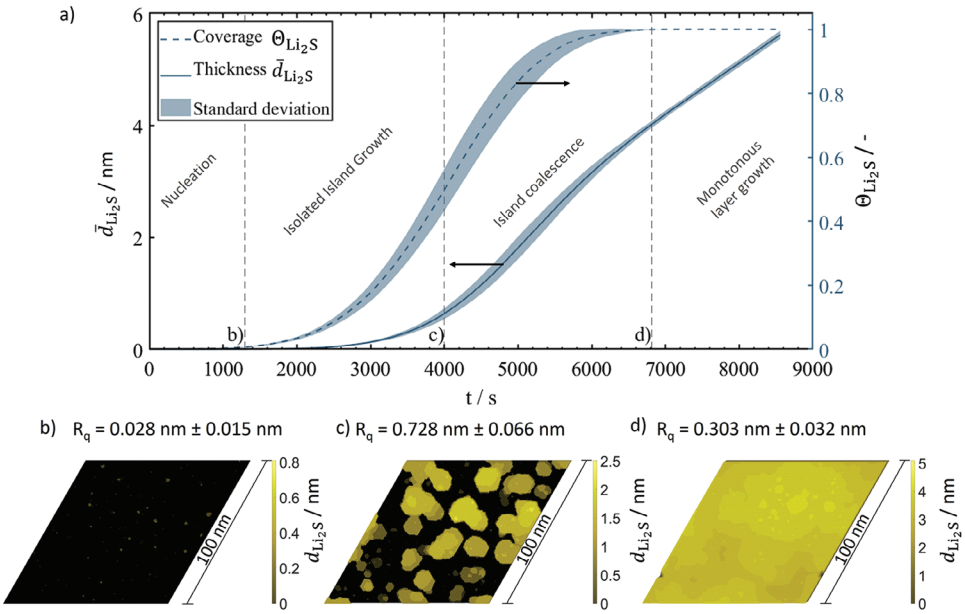

Figure 2. Evolution of surface for 1 M LiTFSI electrolyte during discharge: a) evolution of average thickness, $\bar{d}_{Li_2S}$, and of carbon surface coverage by Li_2S precipitate, Θ_{Li_2S}, over time. Surface structure and square root roughness of the surface, R_q, b) at the end of nucleation (1294 s), c) at the end of island growth (4002 s), and d) at the end of island coalescence (6809 s). $c_{S^{2-}} = 6.5 \times 10^{-4}$ mol m^{-3}.

precipitation process by checking the ratio of the transition rates for precipitation versus dissolution at similar sites, that is, with similar Li_2S neighbors: if the ratio is above 1, precipitation occurs; otherwise, precipitates are more likely to dissolve. The probability ratio of precipitation versus dissolution of Li_2S on the carbon surface is significantly below one for less than two precipitated Li_2S neighbors ($\Gamma^{prec}_{C,0}/\Gamma^{diss}_{C,0} = 9.9 \times 10^{-4}$ and $\Gamma^{prec}_{C,1}/\Gamma^{diss}_{C,1} = 0.25$). This makes it unlikely and energetically unfavorable for Li_2S to remain as a precipitate on the surface. As soon as two neighboring Li_2S exist, the ratio rises significantly above 1 ($\Gamma^{prec}_{C,2}/\Gamma^{diss}_{C,2} = 61.45$), therefore precipitation is more likely to happen. After 1294 s, there were sufficient events of Li_2S molecules meeting at the surface to form a stable nucleus that covered the carbon surface by 0.5% (Figure 2b).

This marks the beginning of the second phase, isolated island growth, where the coverage and average precipitate thickness increase exponentially. In this phase, the single islands grow monotonously, reaching diameters of up to 10–20 nm, but heights below 2.5 nm. The islands are then rather flat (Figure 2c). The outer edges of the islands are smooth and rounded, so that the laterally deposited Li_2S molecules are directly incorporated into the island structure, resulting in a uniform, but anisotropic (because more lateral) growth. This LiTFSI-typical growth can again be explained by energy-related process probabilities; precipitation of Li_2S on a single Li_2S site is less likely than dissolution ($\Gamma^{prec}_{Li_2S,0}/\Gamma^{diss}_{Li_2S,0} = 0.04$), whereas precipitation is favored at preexisting kink sites on the carbon surface, for example, $\Gamma^{prec}_{C,2}/\Gamma^{diss}_{C,2} = 61.45$. This implies that lateral growth is energetically more favorable for the LiTFSI electrolyte, and while vertical growth is slower, it is still steadily occurs.

A turning point is reached at a coverage of ≈50%, because islands to collide more frequently. During this phase of island coalescence, the coverage curve's slope decreases to zero until it reaches full surface coverage, as shown in Figure 2d. During island coalescence, the thickness initially grows exponentially then slows down and becomes linear as it approaches 100% carbon surface coverage. The end of the island coalescence occurs alongside the flattening of the Li_2S surface, where the surface roughness decreases from 0.728 to 0.302 nm. Here, the last phase of monotonous layer growth starts. In the absence of Li_2S interaction with the substrate surface, the energetic preference shifts toward the linear growth of one Li_2S layer after another. Constant current operation will continue until the area is fully passivated and beyond until the tunneling distance is reached.[32] At this point, the voltage will break down, and the constant current operation is not feasible anymore. Our experiment and simulation stop before this point, that is, we can assume constant current and constantly high supersaturation. The here analyzed and modeled precipitation is a chemical process which occurs as long as there is sufficient supersaturation. The relatively flat, homogeneous growth predicted by the simulation resembles the experimentally reported growth mechanism of LiTFSI electrolyte,[8] as indicated in Figure 1b).

The simulation is terminated at all lattice sites when the precipitate thickness is at least 5 nm. After this point electron tunneling through the insulating Li_2S becomes increasingly more difficult. We conclude that the experiment performed for the LiTFSI electrolyte was stopped within the constant growth region.

In order to understand why the morphology is different for LiBr, we will now analyze the simulated progression in morphology, coverage, and layer growth for LiBr electrolyte, shown in **Figure 3**.

The growth stages of Li_2S for LiBr in Figure 3a resemble that of Li_2S for LiTFSI electrolyte: an initial nucleation phase

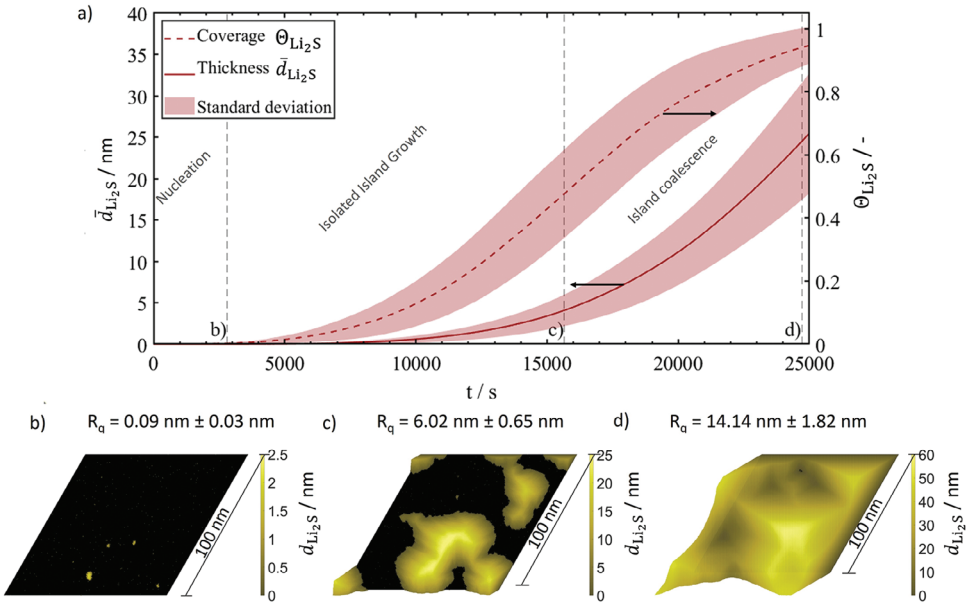

Figure 3. Evolution of surface for 1 M LiBr electrolyte during discharge: a) evolution of average thickness, $\bar{d}_{Li_2S}$, and of carbon surface coverage by Li_2S precipitate, Θ_{Li_2S}, over time. Surface structure and square root roughness of the surface, R_q, b) at the end of nucleation (2802 s), c) at the end of island growth (15 660 s), and d) at the end of island coalescence (24 750 s). $c_{S^{2-}} = 40$ mol m^{-3}.

without precipitation, followed by a steep increase in thickness and a flat increase in coverage in the isolated island growth phase; after reaching 50% coverage, a turning point in coverage starts the island coalescence phase with a slow transition to linear thickness growth. In contrast to LiTFSI, the isolated island growth phase starts later, that is, after 3000 s (Figure 3b) instead of 1200 s. The longer time to form stable nuclei can be explained by the lower precipitation-to-dissolution probability ratios of Li_2S on carbon that result from the lower binding energy of Li_2S to the carbon surface (e.g., $\Gamma^{prec}_{C,2} / \Gamma^{diss}_{C,2} = 0.2$ for LiBr versus 65 for LiTFSI). For LiBr, at least 3 neighboring Li_2S are required to get a higher probability ration of precipitation versus dissolution: $\Gamma^{prec}_{C,3} / \Gamma^{diss}_{C,3} = 1.58$.

A significantly higher average thickness is reached in the phase of isolated island growth, especially during the island coalescence phase, compared to the growth with LiTFSI electrolyte. At the end of both phases, the average thickness is approximately five times higher s for the LiBr electrolyte compared to the LiTFSI electrolyte. This increase is related to the evolution of a more uneven Li_2S morphology at the carbon surface, as seen in Figure 3c,d. At 50% coverage, large particles of semi-spherical shape are visible, with islands being similarly high and wide.

The largely uneven surface coverage is quantitatively visible with large surface roughnesses of 6.02 nm (Figure 3c) to 14.14 nm (Figure 3d). These are more than 8 and 40 times larger, respectively than that obtained for LiTFSI. The result is a surface structure with a highly accessible carbon surface and therefore a low surface passivation. When all carbon sites are covered by at least 5 nm (termination condition), which happens ≈25 000 s, the average thickness was found to be 26 nm versus 5 nm in the case of LiTFSI case. This corresponds to a significantly higher amount of precipitated Li_2S. The uneven surface structure causes slower passivation, leading to the experimentally observed doubling of capacity with LiBr (cf. Figure S1, Supporting Information).

Simulations further revealed a phenomenon with practical implications: coverage and average thickness show a higher standard deviation for LiBr compared to LiTFSI electrolyte (colored areas in Figures 2a and 3a). The morphology and properties of the precipitate might deviate significantly, suggesting likely stronger fluctuations in Li_2S morphology along the cell thickness for the LiBr electrolyte and on the resulting electrode performance. For LiBr, thickness variation increases monotonously with time, whereas for LiTFSI it becomes negligible at the end of discharge. Due to the low precipitation-to-dissolution probability ratios on carbon for LiBr, the time to form stable Li_2S nuclei fluctuates strongly. Finally, the high fluctuations could also mean that the semi-spherical Li_2S particles occur at different sizes. In Figure 3c, smaller particles with 10 nm thickness sit beside a large structure of 25 nm. The underlying strong fluctuations in growth rates between particles and in morphology can again be explained by energetic considerations.

For this, we have a deeper look into the impact of morphology, that is, the number of neighbors and supersaturation on the growth rates. Assuming a saturated, but not oversaturated, solution which corresponds to a dimensionless, supersaturation-dependent Gibbs energy of $\beta = 0$ (see Equation (8)), precipitation and dissolution on a kink site with three neighboring Li_2S, that is, $i = 3$, are equally likely for both electrolytes (see Equations (1)–(2)). The interface between the crystal and the solution decreases in configurations with more than three lateral neighbors, however, it increases in configurations with fewer than three neighbors. For sites with more neighbors or for supersaturated solutions (dimensionless Gibbs energy $\beta > 0$), the probability ratio is shifted toward Li_2S precipitation. Meaning, the Li_2S precipitate grows after a stable Li_2S nucleus is formed. It is worth

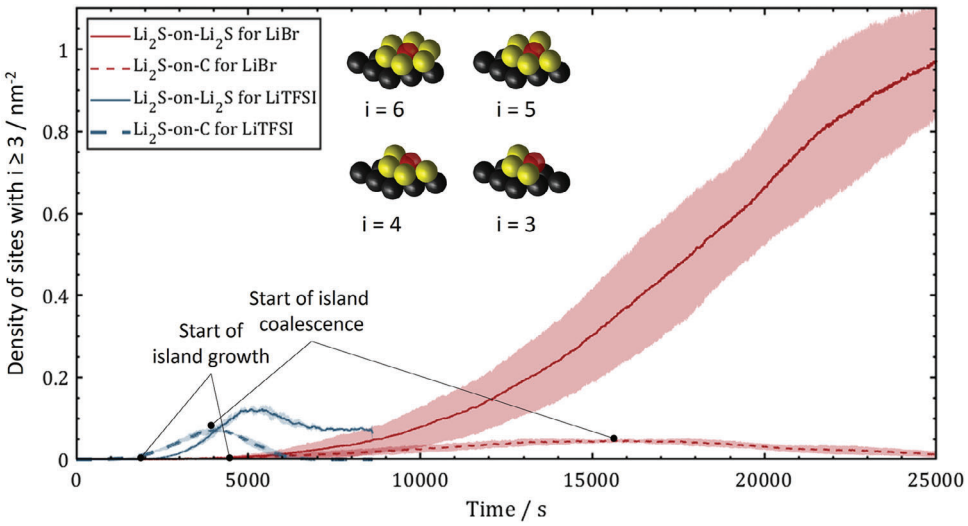

Figure 4. Impact of electrolyte salt on the evolution of the density of sites with at least three lateral neighbors, $i \geq 3$, for Li_2S on carbon or Li_2S sites. S^{2-} concentration of 6.5×10^{-4} mol m^{-3} (equal to $\beta = 13.38$) for LiTFSI electrolyte and of 40 mol m^{-3} (equal to $\beta = 4.21$) for LiBr electrolyte. The colored area denotes the standard deviation for five individual simulation runs.

investigating the progression of available lateral next neighbors (NN) for Li_2S molecules during the precipitation process on carbon and Li_2S, respectively. For the here-analyzed conditions with S^{2-} concentration of 40 and 6.5×10^{-4} mol m^{-3}, which corresponds to $\beta_{LiBr} = 4.21$ and $\beta_{LiTFSI} = 13.38$, three or more neighbors are sufficient. **Figure 4** shows the evolution of the density of lattice sites with at least three neighbors for the two electrolytes.

For both LiTFSI and LiBr, the density of stable Li_2S sites ($i \geq 3$) commences at carbon only after entering the previously discussed phase of island growth following 1294 and 2802 s, respectively. For Li_2S with less than three neighbors, the probability of precipitation is lower than the probability of dissolution, leading to unstable Li_2S sites on the carbon (see Supporting Information). The site density for $i \geq 3$ on carbon reaches a maximum when the Li_2S islands start to coalesce. It subsequently decreases due to the increasing carbon surface coverage. The maximum site density for the LiBr electrolyte on carbon is 50% smaller than that of the LiTFSI electrolyte, which means that fewer Li_2S islands were formed on carbon for LiBr. This can be seen in Figure 2c, where many more individual islands are present in the LiTFSI electrolyte. Once the density of Li_2S on the carbon surface drops to zero, there is no accessible carbon surface ($\Theta_{Li_2S} = 1$).

The density of sites for a given number of neighbors needs to be multiplied with the respective next neighbor-dependent rate to determine the overall probability of surface growth. For LiTFSI, precipitation on carbon is >1300 times more likely than dissolution, while precipitation on carbon is much less likely for LiBr ($\Gamma^{prec}_{C,3}/\Gamma^{diss}_{C,3} = 1.58$, $\Gamma^{prec}_{C,4}/\Gamma^{diss}_{C,4} = 11.84$, $\Gamma^{prec}_{C,5}/\Gamma^{diss}_{C,5} = 88.84$). This explains why Li_2S in the LiTFSI electrolyte covers the carbon surface rapidly after the onset of island growth, whereas the deposition of Li_2S on the carbon in the LiBr electrolyte is slow because it is energetically unfavorable.

Figure 4 also reveals a large difference between site density on Li_2S versus carbon. In LiTFSI electrolytes, the density of sites on Li_2S with at least three Li_2S neighbors rises later and slower than on carbon. Furthermore, the site density reaches a maximum toward the end of the island coalescence phase and stays relatively constant after a slight drop. This indicates a shift to a rather homogenous linear layer growth once the carbon surface is nearly covered, as shown in Figure 2. The complete coverage of carbon with Li_2S contributes to the constant density and homogeneous growth because almost all Li_2S nucleation and island growth occurs on Li_2S. In contrast, in the LiBr electrolyte, the density on Li_2S of sites with at least three Li_2S next neighbors increases immediately after the start of island growth, that is, simultaneously with growth on carbon and then it grows exponentially. The large difference between the monotonous site density growth on Li_2S for LiBr and the evolution of a maximum for LiTFSI can be attributed to the following; once a stable nucleus is formed in LiTFSI, the energetically favored crystal-solution interface is used to proceed with the precipitation of Li_2S until the full layer is covered. It is very unlikely that new Li_2S nuclei will form on Li_2S in the course of island growth due to the high energy cost of creating a new crystal-solution interface. Since the probability of Li_2S precipitation on a new layer is much lower than precipitation in a layer that is already filled with Li_2S this leads to lateral growth. In the LiBr electrolyte, the probability for the precipitation of Li_2S on carbon with three neighboring Li_2S is only slightly higher than the probability of dissolution. Moreover, the difference between the probability of precipitation on itself to that on carbon is several magnitudes higher. As a result, Li_2S favors precipitation on a newly formed Li_2S layer instead of on the lowest carbon layer. This results in a continuous increase in the density of sites of Li_2S-on-Li_2S that leads to growth in the height of Li_2S structures instead of lateral growing.

In summary, surface morphology and passivation can be influenced by electrolyte properties because they change the attraction of the Li_2S to carbon and precipitated Li_2S. High solubilities reduce the probability of precipitation, which further decreases on foreign substrates. This results in high 3D structures and reduced passivation, as in the case of the LiBr electrolyte. In the following section, we investigate how changes in electrolyte

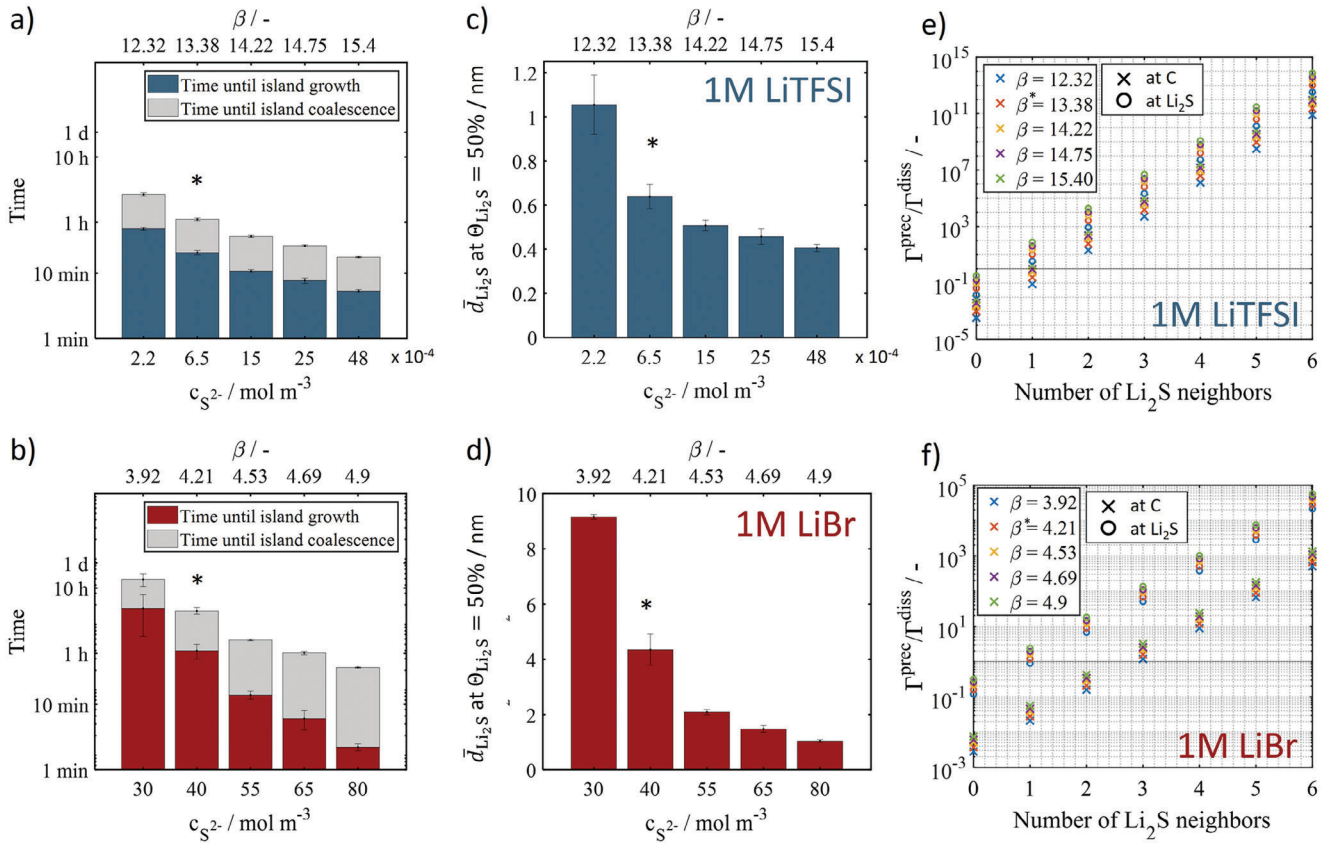

Figure 5. Impact of supersaturation, represented by S^{2-} concentration, $c_{s^{2-}}$, and β, for LiTFSI and LiBr electrolyte on precipitation: time until the start of island growth ($\Theta_{Li_2S} = 0.5\%$) and island coalescence ($\Theta_{Li_2S} = 50\%$) for a) LiTFSI and b) LiBr; the average thickness at 50% coverage $\bar{d}_{Li_2S}$ for c) LiTFSI and d) LiBr. Error bars represent the standard deviation computed from five simulations. Probability ratio of precipitation to dissolution of adsorbed Li_2S, $\Gamma^{prec} / \Gamma^{diss}$, depending on the number of adsorbed Li_2S neighbors for different supersaturation β in e) LiTFSI electrolyte and f) in LiBr electrolyte. $\Delta P = 3.75$ * denotes the concentration of the reference scenario.

conditions and substrate properties impact the observed precipitation behavior. This will further reveal the potential for tuning of precipitation and enable the assessment of the effect of changes in operating conditions.

2.3. Influence of Supersaturation

The supersaturation of a solution, and therefore the supersaturation-dependent dimensionless Gibbs energy β, is the driving force for crystallization,[31,33,34] The degree of supersaturation with Li_2S is dependent on the concentration of Li^+ and S^{2-} ions. The previously used S^{2-} concentration during precipitation of LiTFSI and LiBr electrolytes was adjusted to the experimentally measured 0.05C discharge rates, and a constant concentration was assumed during the second discharge plateau, that is, during precipitation. Supersaturation may change when changing battery chemistry or operation, which is what we analyze in the following. In particular, the S^{2-} concentration level depends on the S^{2-} production and precipitation rate. The former can be directly influenced by the discharge rate.[17]

A linear proportionality of the S^{2-} concentration to discharge rate cannot be assumed, because of the complex behavior and varying concentrations of the intermediate polysulfides,[17,20] Yet, it is reasonable to assume that an increase in discharge rate leads to a higher S^{2-} concentration in the electrolyte bulk, ultimately resulting in more supersaturation. To analyze the impact of the discharge rate on the precipitation, the dimensionless Gibbs energy β, which is proportional to the logarithm of the electrolyte supersaturation, was reduced by 8% and increased by 16% compared to the reference values identified for 0.05C. The high values represent higher C-rates.

Figure 5 shows the effects of supersaturation on precipitation time and on the obtained structures. The duration until the onset of Li_2S island growth, represented by $\Theta_{Li_2S} = 0.5\%$, and of island coalescence, represented by $\Theta_{Li_2S} = 50\%$, is depicted in Figure 5a for LiTFSI and in Figure 5b for LiBr electrolyte. The duration decreases with increasing S^{2-} concentration, that is, supersaturation. This is because a higher supersaturation increases the chemical potential difference and consequently the probability of Li_2S precipitation on carbon and on itself. Hence, with high supersaturation, less time is required until enough stable nuclei are formed, and the islands grow. The precipitation rates at low supersaturation are substantially diminished and require a high number of next neighbors on the carbon surface in order to form a stable nucleus. In this case, it takes a very long time for such

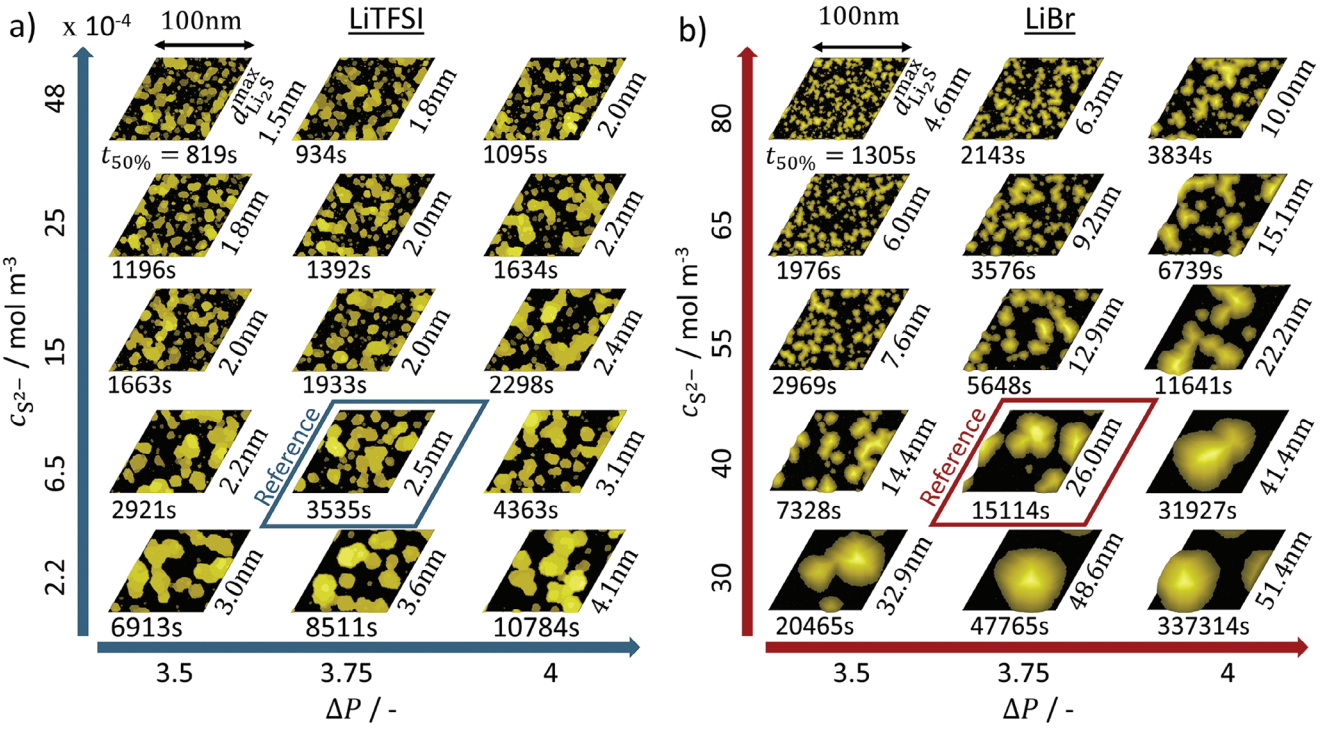

Figure 6. Li_2S surface morphology, time until reaching the island coalescence phase ($\Theta_{Li_2S} = 50\%$) reaching a surface coverage of 50%, $t_{50\%}$, and maximum local Li_2S precipitate thickness, d_{max} for varying supersation (represented by $c_{S^{2-}}$) and changes in substrate binding energy, represented by the interfacial difference parameter, ΔP from 3.5 to 4 for a) LiTFSI and b) LiBr electrolyte. Reference configurations are marked by a square. Note: A higher value of ΔP corresponds to lower binding energy on the substrate.

a state to occur. For all concentrations in the LiTFSI electrolyte, the time until islands coalesce is 3.3 times that for island formation. For LiBr, the relative time interval from island growth to coalescence is even higher, so that at a high S^{2-} concentration of 80 mol m^{-3}, it takes 16 times longer for the islands to coalesce than to form stable nuclei, compared to twice at low S^{2-} concentration of 30 mol m^{-3}.

As the S^{2-} concentration increases, the probability of precipitation versus dissolution increases, ultimately reducing overall growth time. This is shown for LiTFSI in Figure 5e and for LiBr in Figure 5f. In all cases, the probability is higher for higher saturations. It also increases with the number of neighbors and is higher for precipitation on Li_2S than on carbon. The impact is more pronounced for LiBr. In LiBr electrolyte, the probability ratio for the precipitation of Li_2S on Li_2S with one neighbor ($i \geq 1$) exceeds one only for high supersaturations. In contrast, the same ratio is far below 1 for precipitation on carbon. It needs at least three neighboring Li_2S for the probability ratio to exceed one, that is, to build stable and grow precipitates also on carbon; supersaturation increases the probability significantly due to more Li_2S being able to adsorb. With the high concentration, the nuclei occur more frequently, which shortens the time until island growth. However, they are relatively unstable due to the still high probability of dissolution, which results in the observed long duration required for a significant part of the surface to become covered ($\Theta_{Li_2S} = 50\%$). With the high probability for growth on Li_2S, this leads to fewer and larger particles for high concentrations (cf. **Figure** 6b).

In LiTFSI, the Li_2S precipitation on carbon can occur with only one Li_2S neighbor ($i \geq 1$), yet it requires high supersaturation, which explains the decreasing growth time with supersaturation. From two Li_2S neighbors onward, precipitation is likely for all concentrations and substrates. Therefore, not only nuclei formation but also growth and coalescence on carbon are facile and rapid, even for low concentrations. Growth times are therefore less sensitive to concentration. Because the probability ratio is quite close on carbon and Li_2S, Li_2S precipitates on both, leading to many flat particles (Figure 6a). Increasing concentration leads to more and smaller particles.

The average precipitate thickness is used to quantify the amount of Li_2S precipitate. It is shown in Figure 5c,d at the start of island coalescence. Thickness decreases for higher supersaturation for both electrolytes. Again, the sensitivity to supersaturation is more pronounced for LiBr electrolytes. For LiBr, the thickness is 9 times smaller for the maximum versus minimum supersaturation, while for LiTFSI it is only 2.5 times smaller. For the largest supersaturation of LiTFSI electrolytes, the thickness is 0.4 nm, which corresponds roughly to the height of one Li_2S molecule. This shows that precipitation is preferred on the carbon surface before a second layer is formed. In general, at such high supersaturation, single Li_2S molecules tend to form more nuclei and small islands rather than large, connected islands. This can be seen in the morphology snapshots at 50% coverage in Figure 6. When decreasing supersaturation, the island density at 50% coverage decreases due to wider islands for LiBr electrolyte and coalesced islands for LiTFSI. The increase in

island size and coalesced islands with lower supersaturation are well visible in the morphology snapshots. For LiBr at the lowest concentration, even only one single island is visible in an area of 100 nm × 100 nm, with the corresponding average precipitate thickness of ≈9 nm. In contrast, flat structures occur with LiTFSI because the probability for Li_2S precipitation on carbon is high for more than 2 next neighbors, both on the carbon surface and on itself (cf. Figure 5e).

This leads to the conclusion that low supersaturation, and thus low C-rates, lead to larger particles, longer run times, and less surface passivation. This trend occurs for both LiBr and LiTFSI, though with stronger intensity for LiBr. The low supersaturation leads to long nucleation times; allowing the carbon surface to remain free of the electrically insulating Li_2S for an extended period of time. At low supersaturation, fewer islands with higher Li_2S precipitates are formed, which also keeps the carbon surface free of Li_2S for longer during precipitation.

2.4. Growth Control via Substrate Properties

The substrate in LSB cathodes provides the electrons for the electrochemical reduction of sulfur and polysulfides, and it interacts with Li_2S, which precipitates on its surface. Changing the properties of the substrate will change the binding energy to Li_2S, and ultimately the Li_2S surface structure during precipitation, sulfur utilization, and discharge capacity. Various strategies to modify the binding energy between substrate and polysulfides have already been investigated in the literature.[35] Increasing the binding energy of polysulfides and Li_2S to the substrate by doping the surface reduces shuttle effects.[15] Substrate materials with high and low binding energies were experimentally proven to affect the surface morphology differently.[36] This motivates tuning the surface properties to achieve better Li_2S precipitate morphologies and cell performance.

In the following, we elucidate the effect of surface tuning on the precipitation process and the resulting morphology. For this purpose, stronger and weaker binding substrate material is investigated by varying the interfacial difference parameter, ΔP, by 6.6%. A lower binding energy of Li_2S on carbon, and thus a lower probability of precipitation and higher probability of dissolution, corresponds to a larger ΔP (see Equations (3) and (4)). The effect of the substrate binding energy of Li_2S on the substrate and Li_2S supersaturation, that is, discharge rate, on the morphology is displayed in Figure 6 for three different ΔP and each of the electrolytes.

The figure shows the impact of S^{2-} concentration, that is, supersaturation, and interfacial difference parameter ΔP on the Li_2S surface morphology for LiTFSI and LiBr electrolytes at the start of island coalescence ($\Theta_{Li_2S} = 50\%$). Further, it provides the corresponding elapsed growth time and the largest obtained local thickness. For further results, see Supporting Information. A weaker binding energy ($\Delta P = 4$) increases the growth time and the maximum thickness compared to the reference conditions ($\Delta P = 3.75$, marked with a square). This trend holds for all supersaturations and salts. The increase is more pronounced for LiBr: On weak binding substrates, a single particle can be observed that is 1.6 times higher (max. 41.4 nm) and 1.5 times larger in diameter compared to the Li_2S particles at the reference scenario. The number of particles has approximately halved. This behavior can be explained by analyzing the ratio between the precipitation rate and the dissolution rate for sites with three neighbors: increasing the binding energy, that is, decreasing the interfacial difference parameter, yields higher precipitation-to-dissolution probabilities on carbon, with $\Gamma^{prec}_{C,3}/\Gamma^{diss}_{C,3} = 1.23$ for $\Delta P = 4$, 1.58 for $\Delta P = 3.75$, and 2.03 for $\Delta P = 3.5$ (cf. Figure S2, Supporting Information), all at reference concentration. The probability of new nuclei forming is 40% lower for $\Delta P = 4$ compared to the reference scenario, accordingly, there is a higher likelihood for precipitated molecules to dissolve. In contrast, Li_2S-on-Li_2S precipitation and dissolution are ΔP independent (Equations (1) and (2)), and growth is energetically more favorable on Li_2S than on carbon ($\Gamma^{prec}_{Li_2S,3}/\Gamma^{diss}_{Li_2S,3} = 67$), which allows for the growth of large particle-like structures with low surface passivation.

Decreasing both supersaturation and binding energies causes growth time and precipitate thickness to reach the highest values, and particles become less numerous. The lowest supersaturation and binding energy yield huge particle-like Li_2S structures with up to 51.4 nm thickness for LiBr, and for LiTFSI, flat Li_2S islands with a maximum thickness of 4.1 nm and widths ≈20 nm. For LiTFSI electrolytes, the influence of supersaturation is more pronounced than the influence of the binding energy of the substrate material. Changing the S^{2-} concentration from 2.2×10^{-4} to 48×10^{-4} mol m^{-3} doubles the thickness and diameter of the Li_2S islands for all ΔP. In contrast, changing the binding energy of substrate material shows minor changes in the Li_2S morphology and only a 33% increase in diameter and thickness. The relatively small impact of the binding energy on Li_2S growth and morphology for LiTFSI is again attributed to the precipitation versus dissolution properties; the probability ratios of precipitation versus dissolution for Li_2S on the substrate material are close to the probability of Li_2S on Li_2S, resulting in a flat growth of Li_2S islands. However, a strong increase of ΔP, so that the repulsive behavior of the substrate to Li_2S becomes stronger, could provide a change in the growth structure.

ΔP has a stronger impact for LiBr; with increasing supersaturation, LiBr shows a significant influence of ΔP on the Li_2S structure. More single Li_2S islands with 4–5 nm thickness are formed for the highest of S^{2-} concentrations and highest binding energy at $\Delta P = 3.5$. Compared to this, double the average thickness can be observed for the lowest binding energy at $\Delta P = 4$ at the same concentration. This reduction of the binding energy from $\Delta P = 3.5$ to 4 decreases the probability of precipitation to dissolution on carbon by ≈65%; resulting in fewer, but larger islands, that are doubled in height and width.

In conclusion, both electrolytes show the same trends: for low supersaturation, that is, discharge rates and weakly Li_2S-binding substrates, passivation is delayed and high Li_2S precipitate thickness is observed. This effect is larger for electrolytes with a high Li_2S solubility, as shown here for LiBr electrolytes. As a lower passivation and longer operating time is desired for discharge, this suggests that supports with lower binding affinities are preferable.

In any case, a strong sensitivity of the precipitate morphology and discharge performance to a change in substrate properties is expected, especially for high donor number electrolytes.

3. Conclusion

Surface passivation due to the insulating nature of Li_2S is a crucial challenge for LSBs Controlling it requires a thorough understanding of the fundamental processes involved. The kMC model presented here provides unprecedented insight into the precipitation behavior of Li_2S on the carbon surface and the resulting surface passivation for different electrolytes, substrate properties, and discharge rates. It is able to explain the experimentally observed changes in Li_2S morphology and passivation state at 0.05C discharge rate by using the material properties of either LiTFSI or LiBr electrolyte: The difference in solubility of Li_2S in the electrolytes leads to drastic changes in the interaction energy between Li_2S on substrate as well as Li_2S on itself, resulting in different probabilities where Li_2S is more likely to precipitate. For the LiTFSI electrolyte, the nucleation probability on a carbon substrate is fast because even two neighboring Li_2S are sufficient, that the precipitation rate is faster than the dissolution rate. This causes fast nucleation and lateral growth, leading to capacity losses during discharge due to fast passivation of the electrochemically active carbon surface and, thus, to low sulfur utilization. In contrast, large particle-like Li_2S structures are formed in the LiBr electrolyte, leading to slower passivation. This can be attributed to the low interaction energy between the carbon surface and Li_2S. The precipitation rate is faster than the dissolution rate only when six or more neighboring Li_2S molecules are present at the surface. Correspondingly, nucleation and lateral growth on carbon, and consequently passivation, is slow compared to Li_2S-on-Li_2S growth, where only two molecules are needed to get a higher probability of precipitation to dissolution.

At higher discharge currents, more S^{2-} is produced, resulting in higher supersaturation. The increased S^{2-} concentration increases the chemical driving force for Li_2S precipitation, which causes faster nucleation, growth, and passivation. For both electrolytes, a high discharge rate is disadvantageous because significantly smaller Li_2S islands are formed on carbon, which subsequently quickly coalesce and passivate the surface. The LiBr electrolyte performs comparably better at high discharge rates because larger structures are formed. Consequently, electrolytes with higher Li_2S solubility are able to improve the discharge capability for high rates.

Using substrate materials other than carbon or modifying carbon surface properties in the sulfur electrode changes the binding energy between Li_2S and the substrate. This, in turn, changes the difference in precipitation rates on substrate versus on Li_2S itself. The influence of the substrate properties is particularly pronounced at low concentrations, that is, discharge rates. When Li_2S binds more strongly to the substrate, number of nuclei increases, thus Li_2S precipitates become smaller and more numerous, accelerating passivation. The sensitivity to substrate properties is especially pronounced for the LiBr electrolyte: low supersaturation with low binding energies causes large Li_2S semispherical particles, whereas high supersaturation with high binding energies causes flat Li_2S precipitates. Note that modifying the substrate-Li_2S binding may also modify the binding energy to polysulfides.[35] An interesting way to control morphology and prevent early surface passivation may be to design supports or the support surface with regions of more strongly binding materials, which serve as nucleation points. They allow to influence the substrate-Li_2S binding energy and enable the precise control of Li_2S morphology. Examples for such surface modifications are catalysts on the substrate surface,[37,38] We propose to analyze such supports in combination with electrolyte design to tailor both, Li_2S precipitation and polysulfide attraction close to the surface.

Our model-based analysis has given significant new insights into how, why, and when the surface passivates in lithium–sulfur cathodes, and that promising strategies to mitigate this effect are the manipulation of electrolyte composition, supersaturation, that is operating current, and surface properties. This shows that the electrolyte design needs to move toward a LiBr electrolyte in combination with a weakly binding substrate material. The here presented trend of getting more flat structures for LiTFSI than for LiBr growth structure in DME solvent can be confirmed by Chu et al.[28] using the same conducting salt in a solvent consisting of DOL: DOL. A slightly lower Li_2S solubility than LiBr but much higher solubility than LiTFSI electrolyte would result in a few large particles that do not passivate the electroactive surface much. This could be improved by adding a weakly binding substrate material to directly precipitate Li_2S onto the existing Li_2S, leaving the surface free for longer,[6,36] In addition, the model demonstrates capability in analyzing electrolytes with different solubilities, and thus DN numbers; by this, it allows to assess influencing factors such as the conductive salt anion (this work), solvent,[39] additives,[40] and conductive salt concentration.[41]

Further, Yan et al.[42] and Lang et al.[7] suggested that performance is also hampered by Li_2S_2 as a poorly soluble and insulating intermediate. On the other hand, Liu et al.[11] suggested Li_2S as the predominant species. Studies using an extended kMC model may check, under which conditions Li_2S_2 plays a significant role.

The kMC model may also be extended in the future to a multiscale model by coupling it with a continuum model of electrodes or cells. This would allow for the analysis of the effect of polysulfides with a more complex reduction mechanism,[20] and of concentration, current and potential distribution within the electrode. We have applied such models for the reactive formation of the SEI in LIBs and revealed uneven film formation as a function of current, and the effect of concentration on film composition and morphology,[27,43] The here presented kMC model thus provides an important base for further studies regarding performance and passivation in sulfur cathodes.

4. Methods

This work focused on the comparison of Li_2S growth and emerging structures at carbon substrates in LSBs with two different liquid electrolytes. Methods proposed by Binsbergen et al.[30] and refined by Rak et al.[31] for crystal growth from solution were used to describe the growth mechanism. Simulated results were compared with electrochemical measurements prepared by discharging coin cells and post-mortem images of the carbon surface structure with a scanning electron microscope (SEM). Further details are described in the following section.

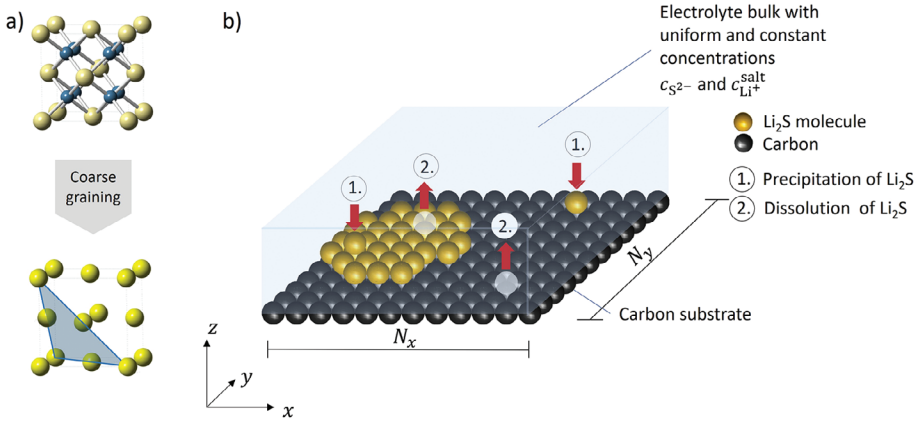

Figure 7. a) Coarse graining of Li_2S antifluorite structure to face cubic centered single atom crystal structure, and b) overview of processes at the carbon/electrolyte interface, including precipitation and dissolution of Li_2S taking place in the kinetic Monte–Carlo model.

4.1. Experimental Set-Up

Cathode Preparation: The carbon nano fiber (CNF) electrodes were prepared by electrospinning. First, 1 g of polyacrylonitrile (PAN, Mw = 150 000, Sigma-Aldrich) was dissolved in 10 mL *N,N*-dimethylformamide (DMF, Sigma-Aldrich) and stirred for 12 h. This uniform polymer solution was filled in a syringe (21 gauge) and an electric field (17 kV) was applied between the syringe and aluminum (Al) foil collector to electrospun with a 1 mL h^{-1} feeding rate. The electrospun membrane was detached from Al foil, dried overnight in an oven at 60 °C, and punched into 18 pi disk size. The membrane was stabilized in ambient air for 3 h at 220 °C, followed by carbonization at 800 °C under N_2 flow conditions for 1 h. After cooling, the polysulfide/CNF electrode was prepared by drop-casting 40 µl of an 0.2 M Li_2S_8 solution onto the CNF electrode, corresponding to 2 mg cm^{-2} loaded cathode. Li_2S_8 solution was prepared by mixing and heating lithium sulfide (Li_2S, Sigma-Aldrich) and octa-sulfur (S_8, Sigma-Aldrich) powder) with a stoichiometric amount to prepare a Li_2S_8 solution.

Electrolyte Preparation: The electrolyte was prepared in an argon-filled glove box by dissolving 1 M lithium salt (Li*X*, *X* = TFSI or Br) in 1,2-dimethoxyethane (DME).

Electrochemical Measurements: The electrochemical properties were evaluated using a 2032-type coin cell. A Li foil (450 µm, Honjo Metal) punched with Ø 16.5 mm size was inserted, and a Celgard 2400 monolayer polypropylene membrane (Ø 18 mm) was used as a separator. WBC300L (Wonatech) automatic battery cycler was used to perform the galvanostatic charge and discharge test.

Characterization: Li_2S deposition morphologies were observed using scanning electron microscopy (SEM, Magellan 400, FEI Co.).

4.2. Mathematical Model

The model simulated how Li_2S, as the discharge product of LSBs, was deposited at the substrate surface. Carbon was the substrate material within the cathode onto which an antifluorite Li_2S crystal structure was formed. Following previous work by Liu et al.,[14] the crystal structure was coarse-grained to a face-centered cubic structure, with single Li_2S units occupying an area the size of a sulfur atom (see **Figure** 7a). A Li_2S molecule with diameter ΔL occupied a site of equal lattice size. Lithium ions, geometric orientation, and bond angle of the molecule were neglected, so it was possible to model the predominant (111) surface growth direction of the crystal,[11,12] A Li_2S molecule could precipitate when there was a solid molecule in the layer below it (*z*-direction) and if the probability of precipitation was high enough depending on the number of neighboring Li_2S (below or in x or *y*-direction). As customary for kMC simulations,[44,45] the carbon substrate structure was assumed to have the same lattice size and crystal structure as the growing crystal structure. The concentration of lithium-ions c_{Li^+} and of sulfide ions $c_{S^{2-}}$ in the electrolyte bulk was kept constant throughout the simulation, which was a reasonable assumption due to the low discharge rate below 0.5C. It was reported by Ghaznavi et al.[17] that for discharge rates at 0.5C and below, a constant polysulfide concentration could be assumed. At such low discharge rates, a uniform distribution of all species in the cell could be achieved by diffusion.[17] The dissolved species in the electrolyte were therefore evenly distributed, and the sites at the interface had the same conditions as those in the electrolyte bulk. Furthermore, bond energies between all deposited Li_2S and neighboring solid Li_2S and carbon molecules were considered uniform in all directions.

A 2D + 1 kMC modeling approach, as depicted in Figure 7b, was used to investigate the interaction of processes at the carbon surface, which lead to surface passivation by Li_2S precipitates during discharge. The two lateral dimensions were *x* and *y*, and growth and molecule movement were just possible in the z direction. There were four transition events taking place; precipitation and dissolution of Li_2S on both the carbon surface and on solid Li_2S. The transition rates of Li_2S precipitation and dissolution depended on the change of free energy for the transition from one state to another. They might contain three energy terms for the change of energy due to different effects. First, an energy term with a surface roughness factor α_{111} was needed to occupy a site with *i* lateral neighbors by a single molecule. A second energy contribution accounted for the difference in chemical standard potential due to the concentration of dissolved species, represented by β. Finally, there was an energy correction term containing ΔP, which accounted for cases where Li_2S precipitated on a foreign structure, that is, carbon, and not on solid Li_2S. This yielded the following transition rates for precipitation

on Li_2S, $\Gamma^{prec}_{Li_2S,i}$, for dissolution of Li_2S, $\Gamma^{diss}_{Li_2S,i}$, for precipitation on carbon, $\Gamma^{prec}_{C,i}$ and for dissolution from the carbon surface $\Gamma^{diss}_{C,i}$:

$$\Gamma^{prec}_{Li_2S,i} = k_t \times \exp\left[-\frac{\alpha_{111}}{6}(3 - i) + \frac{\beta}{2}\right] \quad (1)$$

$$\Gamma^{diss}_{Li_2S,i} = k_t \times \exp\left[\frac{\alpha_{111}}{6}(3 - i) - \frac{\beta}{2}\right] \quad (2)$$

$$\Gamma^{prec}_{C,i} = k_t \times \exp\left[-\frac{\alpha_{111}}{6}(3 - i) + \frac{\beta}{2} - \frac{\Delta P}{2}\right] \quad (3)$$

$$\Gamma^{diss}_{C,i} = k_t \times \exp\left[\frac{\alpha_{111}}{6}(3 - i) - \frac{\beta}{2} + \frac{\Delta P}{2}\right] \quad (4)$$

with the number of lateral next neighbors in the same x–y-plane $i \in \mathbb{N}$ with $0 \leq i \leq 6$ and either precipitation or dissolution on Li_2S or carbon. k_t is the frequency factor and is usually used for parametrization to experiments.[46] It was assumed to be independent of the site position and similar for both events.[31] The first term, containing the surface roughness factor α_{111} represented the free energy required to cause the change in the surface structure of the solid–liquid interface. It accounted for the interaction energy between solid and liquid phases for a given lattice site and the number of its lateral neighbors, which was a maximum of six for a crystalline (111) fcc facet. As the interaction energies were not sufficiently available in the literature, the approach for crystals grown from solution by Davey and Elwenspoek who considers an ideal solution with a solubility of Li_2S in the electrolyte expressed as molar X_{Li_2S} was followed:[47,48]

$$\alpha_{111} = \xi_{(111)}\left[\frac{L_{Li_2S}}{RT_{M,\,Li_2S}} - ln\left(X_{Li_2S}\right)\right] \quad (5)$$

with the heat of fusion L_{Li2S}, melting temperature of Li_2S $T_{M,\,Li2S}$, and the crystallographic factor $\xi_{(111)} \times \xi_{(111)}$ was calculated by dividing the number of lateral neighbors in a crystal by the number of total neighbors. For (111) facets, which had six lateral neighbors, and three on top and three below, this yielded a value of $\xi_{(111)} = 0.5$. R is the universal gas constant. The molar fraction was calculated by the concentration of Li_2S in the Li_2S saturated electrolyte with a given conductive salt, $c^{sat}_{Li_2S,j}$ $(j \in \{LiTFSI,\ LiBr\})$, divided by the total concentration of the solution,[49,50]

$$X_{Li_2S,j} = \frac{c^{sat}_{Li_2S,j}}{c_{Solvent} + c^{sat}_{Li_2S,j}} \quad (6)$$

The solvent concentration, $c_{Solvent}$, for DME solvent is calculated as follows.

$$c_{Solvent} = \frac{\rho_{DME}}{M_{DME}} \quad (7)$$

where ρ_{DME} is the density and M_{DME} is the molecular weight of the solvent DME.

The thermodynamic driving force for crystallization was the Gibbs energy of fusion $\Delta\mu$, that is, the chemical potential difference between the solid and solute phases. It was used to calculate the dimensionless energy β as the ratio between the Gibbs energy and the thermal energy RT. Assuming an ideal solution, β can be expressed as the logarithm of the supersaturation ratio of Li_2S. This in turn could be calculated by the fraction of the concentration of dissolved species Li^+ and S^{2-} to the solubility product K_{sp},[31,51]

$$\beta = \frac{\Delta\mu}{RT} = \ln\left(\frac{\left(c^{salt}_{Li^+} + c_{S^{2-}}\right)^2 c_{S^{2-}}}{K_{sp}}\right) \quad (8)$$

here the Li^+ concentration c_{Li^+} contains all lithium ions from the conducting salt and the dissolved Li_2S. Full dissociation was assumed for Li_2S in the solution. The solubility product of Li_2S was calculated from the product of the ion pair concentrations of Li^+ and S^{2-} constituting a saturated solution. Li^+ was taken from the LiTFSI or LiBr conducting salt concentration $c^{salt}_{Li^+}$, and the S^{2-} concentration was equal to the concentration of the fully dissociated Li_2S in a saturated solution of Li_2S.[52]

$$K_{sp} = \left(c^{salt}_{Li^+} + c^{sat}_{Li_2S,j}\right)^2 \times c^{sat}_{Li_2S,j} \quad (9)$$

According to Chu et al.,[8] a fraction (in this study: 1/3) of Li^+ ions were solvated by Br^- ions and did not participate in reactions occurring within the electrolyte and, consequently, also not in the deposition process, which had to be taken into account when using the salt concentration.

The binding energy of Li_2S to the carbon substrate differed from that onto precipitated Li_2S, which was discussed above. To account for precipitation on such chemically foreign substrates, the approach was applied by Binsbergen et al.,[30,53] which introduced the interfacial difference parameter ΔP, to account for the interaction energy of the solid-foreign substrate and liquid-foreign substrate relation. Due to the complexity of calculating the interaction energies, these parameters were estimated from the here presented experiments. A detailed explanation and a discussion of the estimation of the parameter ΔP was given in from the Section 2. A lower binding energy of Li_2S on carbon than on Li_2S precipitated corresponded to a positive ΔP following the procedure of Binsbergen et al.,[30,53]

The kMC algorithm was based on the variable step size method (VSSM),[27,43,44] and structured lists.[54] The (111) fcc lattice has N_x sites in x-direction, N_y in y-direction, yielding $N_{yx} = N_x \times N_y$ carbon sites, on which Li_2S could adsorb from top, that is, from z-direction (see Figure 7b). Precipitation and dissolution of Li_2S were only allowed in the z-direction. As no precipitation or dissolution in the x- or y-direction was allowed, this was a 2+1-D kMC model. Most kMC models used this approach, as they were computationally efficient. At the edges of the lattice, periodic boundaries were implemented. As the concentration in the electrolyte was assumed to be constant and homogeneous, diffusion processes were not resolved. The lattice in the z-direction was dimensioned so that the Li_2S structure could grow sufficiently until reaching the termination condition. The termination condition was fulfilled when the smallest Li_2S thickness reached 5 nm. Above 5 nm, the probability for electron transfer by tunneling strongly diminished,[25,32] making the battery discharge, that is sulfur reduction, stop.

The kMC algorithm for growth and dissolution was as follows:

1) Determine transition rates for precipitation Γ^{prec} or dissolution Γ^{diss} at every surface site (Li_2S,C) accounting for the surface site's number of lateral neighbors.
2) Calculate the sum of transition rates $\Gamma^{\text{tot}} = \sum^{N_{xy}} \Gamma^{\text{prec}} + \sum^{N_{xy}} \Gamma^{\text{diss}}$, which is the sum of all possible processes on a face cubic-centered lattice site of $N_{xy} = N_x \times N_y$
3) Draw a first random number $\zeta_1 \in (0, 1)$.
4) Calculate with ζ_1 the time step Δt for a single event that is determined by:

$$\Delta t = -\frac{\ln(\zeta_1)}{\Gamma^{\text{tot}}} \tag{10}$$

5) Draw a second random number $\zeta_2 \in (0, 1)$.
6) Choose the event, consisting of precipitation or dissolution, at a lattice site and using ζ_2 according to $\sum^{N_{xy}-1} \Gamma^{\text{prec/diss}} < \zeta_2 \Gamma^{\text{tot}} \leq \sum^{N_{xy}} \Gamma^{\text{prec/diss}}$

After each time step Δt, Γ^{tot} was updated by calculating the transition rate on the last changed lattice site, and the time counter was updated: $t_{k+1} = t_k + \Delta t$. Due to the stochastic nature of kMC, each full kMC simulation was repeated 5 times, and average and standard deviation were calculated.

The lattice size was chosen to be 250 × 250, which yielded approximately a surface of 100 nm × 100 nm when assuming a single lattice size of 0.403 nm in the x- and y-direction. See Supporting Information for more information. This lattice size was sufficiently large to avoid artifacts due to numerical stability.

The surface structure and its changes were evaluated by means of average thickness d_{avg}, carbon surface coverage Θ_{Li_2S}, density of nuclei ρ_{island}, and root mean square surface roughness R_q over time; for more information and a full set of parameters see Supporting Information. The frequency factor k_t, S^{2-} concentration $c_{s^{2-}}$, and interfacial difference parameters ΔP were fitted to reproduce the experimentally observed Li_2S growth time and crystal structure.

Supporting Information

Supporting Information is available from the Wiley Online Library or from the author.

Acknowledgements

The authors would like to acknowledge the funding by the Deutsche Forschungsgemeinschaft (DFG, German Research Foundation) under Germany´s Excellence Strategy – EXC 2163/1 – Sustainable and Energy Efficient Aviation – Project-ID 390881007.

Open access funding enabled and organized by Projekt DEAL.

Conflict of Interest

The authors declare no conflict of interest.

Data Availability Statement

Source data are provided with this paper in the KITopen repository after publication at DOI: 10.35097/1954

Keywords

crystal growth, gutmann donor numbers, kinetic monte—carlo (kmc) simulation, lithium–sulfur batteries (lsb), solubilities

Received: July 29, 2024
Revised: September 13, 2024
Published online:

[1] T. Cleaver, P. Kovacik, M. Marinescu, T. Zhang, G. Offer, *J. Electrochem. Soc.* **2018**, *165*, A6029.
[2] S. Evers, L. F. Nazar, *Acc. Chem. Res.* **2013**, *46*, 1135.
[3] J. Schuster, *Angew. Chem., Int. Ed.* **2012**, *51*, 3591.
[4] H. J. Peng, J. Liang, L. Zhu, J.-Q.i Huang, X. B. Cheng, X. Guo, W. Ding, W. Zhu, Q. Zhang, *ACS Nano* **2014**, *8*, 11280.
[5] M. Liu, D. Zhou, Y. B. He, Y. Fu, X. Qin, C. Miao, H. Du, B. Li, Q. H. Yang, Z. Lin, T. S. Zhao, F. Kang, *Nano Energy* **2016**, *22*, 278.
[6] H. Noh, J. Song, J. K. Park, H. T. Kim, *J. Power Sources* **2015**, *293*, 329.
[7] S. Y. Lang, Y. Shi, Y. G. Guo, R. Wen, L. J. Wan, *Angew. Chem., Int. Ed.* **2017**, *56*, 14433.
[8] H. Chu, H. Noh, Y. J. Kim, S. Yuk, J.u-H. Lee, J. Lee, H. Kwack, Y. Kim, D. K. Yang, H. T. Kim, *Nat. Commun.* **2019**, *10*, 188.
[9] S. Y. Lang, R. J. Xiao, L. Gu, Y. G. Guo, R. Wen, L. J. Wan, *J. Am. Chem. Soc.* **2018**, *140*, 8147.
[10] A. A. Franco, in *Li-S Batteries*, World Scientific Publishing Europe Ltd, Europe **2017**, 335–350.
[11] Z. Liu, D. Hubble, P. B. Balbuena, P. P. Mukherjee, *Phys. Chem. Chem. Phys.* **2015**, *17*, 9032.
[12] H. Park, H. S. Koh, D. J. Siegel, *J. Phys. Chem. C* **2015**, *119*, 4675.
[13] Z. Liu, P. B. Balbuena, P. P. Mukherjee, *J. Coord. Chem.* **2016**, *69*, 2090.
[14] Z. Liu, P. P. Mukherjee, *ACS Appl. Mater. Interfaces* **2017**, *9*, 5263.
[15] E. I. Andritsos, C. Lekakou, Q. Cai, *J. Phys. Chem. C* **2021**, *125*, 18108.
[16] V. Thangavel, O. X. Guerrero, M. Quiroga, A. M. Mikala, A. Rucci, A. a. Franco, *Energy Storage Mater.* **2019**, *24*, 472.
[17] M. Ghaznavi, P. Chen, *J. Power Sources* **2014**, *257*, 394.
[18] D. Korff, A. M. Colclasure, Y. Ha, K. Smith, S. DeCaluwe, *J. Electrochem. Soc.* **2021**, *169*, 010520.
[19] A. F. Hofmann, D. N. Fronczek, W. G. Bessler, *J. Power Sources* **2014**, *259*, 300.
[20] P. Schön, U. Krewer, *Electrochim. Acta* **2021**, *373*, 137523.
[21] Y. X. Ren, T. S. Zhao, M. Liu, P. Tan, Y. K. Zeng, *J. Power Sources* **2016**, *336*, 115.
[22] C. Xiong, T. S. Zhao, Y. X. Ren, H. R. Jiang, X. L. Zhou, *Electrochim. Acta* **2019**, *296*, 954.
[23] T. Danner, A. Latz, *Electrochim. Acta* **2019**, *322*, 134719.
[24] G. D. Wehinger, M. Ambrosetti, R. Cheula, Z. B. Ding, M. Isoz, B. Kreitz, K. Kuhlmann, M. Kutscherauer, K. Niyogi, J. Poissonnier, R. Réocreux, D. Rudolf, J. Wagner, R. Zimmermann, M. Bracconi, H. Freund, U. Krewer, M. Maestri, *Chem. Eng. Res. Des.* **2022**, *184*, 39.
[25] F. Röder, V. Laue, U. Krewer, *Batteries Supercaps* **2019**, *2*, 248.
[26] M. Gerasimov, F. A. Soto, J. Wagner, F. Baakes, N. Guo, F. Ospina-Acevedo, F. Röder, P. B. Balbuena, U. Krewer, *J. Phys. Chem. C* **2023**, *127*, 4872.
[27] J. Wagner-Henke, D. Kuai, M. Gerasimov, F. Röder, P. B. Balbuena, U. Krewer, *Nat. Commun.* **2023**, *14*, 6823.
[28] H. Chu, H. Noh, Y. J. Kim, S. Yuk, J.u-H. Lee, J. Lee, H. Kwack, Y. Kim, D. K. Yang, H. T. Kim, *Nat. Commun.* **2019**, *10*, 188.
[29] P. Bennema, J. P. van der Eerden, *J. Cryst. Growth* **1977**, *42*, 201.
[30] F. L. Binsbergen, *J. Cryst. Growth* **1972**, *16*, 249
[31] M. Rak, M. Izdebski, A. Brozi, *Comput. Phys. Commun.* **2001**, *138*, 250.

[32] V. Thangavel, K. H. Xue, Y. Mammeri, M. Quiroga, A. Mastouri, C. Guéry, P. Johansson, M. Morcrette, A. A. Franco, *J. Electrochem. Soc.* **2016**, *163*, A2817.
[33] F. L. Binsbergen, *Kolloid Z. Z. Polym.* **1970**, *238*, 389.
[34] P. Bennema, *J. Cryst. Growth* **1993**, *128*, 97.
[35] H. Li, Y. Li, L. Zhang, *SusMat* **2022**, *2*, 34.
[36] K. Kim, J. Kim, J. H. Moon, *Adv. Sci.* **2023**, *10*, 2206057.
[37] Y. Li, J. Wu, B. Zhang, W. Wang, G. Zhang, Z. W. Seh, N. Zhang, J. Sun, L. Huang, J. Jiang, J. Zhou, Y. Sun, *Energy Storage Mater.* **2020**, *30*, 250.
[38] X. Zhou, J.i Zhou, L. Sun, S. Chen, M. Wang, X. Meng, J. Qu, C. Sun, Z. Z. Yu, Y. Huang, C. W. Bielawski, J. Geng, *ACS Appl. Energy Mater.* **2023**, *6*, 11157.
[39] H. Pan, J. Chen, R. Cao, V. Murugesan, N. N. Rajput, K. S. Han, K. Persson, L. Estevez, M. H. Engelhard, J.i-G. Zhang, K. T. Mueller, Y.i Cui, Y. Shao, J. Liu, *Nat. Energy* **2017**, *2*, 813.
[40] H. Pan, K. S. Han, M. Vijayakumar, J. Xiao, R. Cao, J. Chen, J. Zhang, K. T. Mueller, Y. Shao, J. Liu, *ACS Appl. Mater. Interfaces* **2017**, *9*, 4290.
[41] J. K. Song, M. Kim, S. Park, Y. J. Kim, *J. Energy Chem.* **2023**, *78*, 574.
[42] J. Yan, X. Liu, B. Li, *Adv. Sci.* **2016**, *3*, 1600101.
[43] F. Röder, R. D. Braatz, U. Krewer, *Comput. Chem. Eng.* **2019**, *121*, 722.
[44] M. Andersen, C. Panosetti, K. Reuter, *Front. Chem.* **2019**, *7*, 202.
[45] F. Röder, R. D. Braatz, U. Krewer, *J. Electrochem. Soc.* **2017**, *164*, E3335.
[46] A. M. Reilly, H. Briesen, *J. Chem. Phys.* **2012**, *136*, 034704.
[47] R. J. Davey, *J. Cryst. Growth* **1986**, *76*, 637.
[48] M. Elwenspoek, *J. Cryst. Growth* **1986**, *78*, 353.
[49] C. Park, M. Kanduc, R. Chudoba, A. Ronneburg, S. Risse, M. Ballauff, J. Dzubiella, *J. Power Sources* **2017**, *373*, 70.
[50] J. Szurgot, M. Szurgot, *Cryst. Res. Technol.* **1994**, *29*, 829.
[51] H. J. M. Kramer, G. M. van Rosmalen, *Encyclopedia of separation science*, Academic Press, London **2000**, 64–84.
[52] J. L. Burgot, *Ionic equilibria in analytical chemistry*, Springer, New York **2012**, pp. 1–770.
[53] F. L. Binsbergen, *J. Polym. Sci.* **1973**, *11*, 117.
[54] T. P. Schulze, *J. Comput. Phys.* **2008**, *227*, 2455.